




$5p_{1/2}n\ell_j$ autoionizing states of strontium for $0 \leq \ell \leq 5$ S. Yoshida ¹, J. Burgdörfer,¹ R. Brienza,² G. Fields,² and F. B. Dunning ²¹*Institute for Theoretical Physics, Vienna University of Technology, Vienna A1040, Austria, EU*²*Department of Physics and Astronomy, Rice University, Houston, Texas 77005-1892, USA* (Received 2 December 2022; revised 27 March 2023; accepted 28 March 2023; published 12 April 2023)

We report a comprehensive experimental and theoretical study of the autoionization of core-excited $5p_{1/2}n\ell_j$ strontium Rydberg states for intermediate values of ℓ_j in the range $0 \lesssim \ell_j \lesssim 5$. For a given value of ℓ_j autoionization, which results from the energy exchange between the two excited valence electrons, is found to scale as $\sim 1/n^3$, mirroring the decrease in the Rydberg electron probability density in the vicinity of the inner $5p_{1/2}$ electron cloud. In contrast, the ℓ_j dependence of the autoionization rate is more complex. For the larger values of ℓ_j (≥ 4), the autoionization rate decreases as ℓ_j^{-5} due to the centrifugal barrier, which prevents the Rydberg electron from penetrating the core and inner $5p_{1/2}$ electron cloud. For the low- ℓ_j core-penetrating Rydberg states, the scattering phase shift induced by the effective core potential becomes important in determining both the autoionization rates, which no longer show a monotonic variation with ℓ_j , and the quantum defects.

DOI: [10.1103/PhysRevA.107.043112](https://doi.org/10.1103/PhysRevA.107.043112)**I. INTRODUCTION**

The ground state of an alkaline-earth-metal atom contains two ns valence electrons in a closed outer shell. Rydberg atoms can be formed by exciting one of these electrons to an excited state. Due to their strong tunable interactions with both external electromagnetic fields and neighboring Rydberg atoms, Rydberg atoms find wide application in the study of quantum information and quantum simulation [1,2]. The second electron, however, can also be excited optically to form a doubly excited state [3,4], which opens up additional opportunities. For example, circular Rydberg states can be manipulated optically through laser dressing of the core ion which modifies the polarizability of the Rydberg atom and enables the simultaneous trapping of both Rydberg and ground-state atoms [5–9]. The second valence electron can be used to detect Rydberg atoms through fluorescence imaging [10,11]. One of the key prerequisites for such applications is to understand the interaction between the “inner” excited valence electron and the “outer” Rydberg electron, which shifts the energy levels of the core ion and can lead to autoionization, which provides a convenient means to detect Rydberg atoms [4,12–15]. The sensitivity of the energy shifts and the autoionization rates to the quantum numbers n and ℓ of the Rydberg electron can be exploited to obtain state-selective detection. At the same time, autoionization represents a loss channel and a source of decoherence when studying quantum phenomena.

Autoionization is triggered by energy exchange during a collision between the two valence electrons [4,12]. The autoionization rate can be controlled (and suppressed) by exciting the outer electron to different high- n levels and/or different high- ℓ states. The n -dependence results from changes in the Rydberg electron probability density in the vicinity of the Sr^+ ion core, which decays as $\sim n^{-3}$. In the limit of very-high- n levels the autoionization rate decreases to a level such that radiative decay of the inner excited electron

rather than autoionization limits the lifetime of two-electron-excited states [16]. The competition between radiative decay and autoionization is also of interest in the context of the time-reversed process, dielectronic recombination, in electron-ion collisions which is an important recombination mechanism in many plasmas [17–19]. Such collisions can result in the transient capture of the incident electron through excitation of the ion and the formation of a quasi-bound two-electron-excited state. This state can then either autoionize, thereby regenerating the electron-ion pair, which corresponds to a quasi-elastic electron-ion scattering channel, or can be stabilized by radiative decay of the inner excited electron leading to formation of a neutral atom.

The ℓ dependence of the autoionization rate turns out to be more complex. In the limit of high ℓ , the electron-electron interaction is suppressed because the electrons are separated by the centrifugal barrier and the autoionization rate exhibits a rapid decay with increasing ℓ , scaling as $\sim \ell^{-5}$ [20]. However, even at large distances, the outer electron polarizes the inner valence electron cloud causing small but nonnegligible electron-electron correlations [21,22]. For low quantum numbers n or ℓ , the autoionization rate deviates from these scaling laws due to coupling to perturbers (or intruder states) and the exchange interaction between the two valence electrons. In particular, exchange effects are observed for low- ℓ Rydberg electrons which penetrate the inner valence electron cloud [23]. In this paper we analyze the dependence of the electron-electron interaction on ℓ , covering the range from low- to intermediate- ℓ and identify the onset of the high- ℓ behavior.

Many experimental studies of two-electron-excited states have employed alkaline-earth-metal and alkaline-earth-metal-like atoms [4,11,21,22,24–30] because the wavelengths required for their production can be conveniently generated. For strontium, the $5p_{1/2}n\ell$ autoionizing levels were studied extensively for a wide range of ℓ levels but mostly for states with relatively low values of n , $n < 40$ [4,31–33]. Their study was recently extended to much higher n levels ($280 \lesssim n \lesssim 430$),

but only for $5p_{1/2}np$ and $5p_{1/2}nf$ autoionizing states [16]. In the presence of intruder states, however, the autoionization rates deviate from the $\sim 1/n^3$ scaling and cannot easily be extrapolated to higher n . In the limit of very high ℓ , the outer electron forms a circular state and autoionization becomes negligible [34]. Even if the inner valence electron is excited to a level somewhat above the $5p_{1/2}$ state, Rydberg electrons with values of $\ell \geq 9$ do not penetrate the Sr^+ ion core and autoionization is suppressed. Nevertheless, the wave function of the (polarized) inner valence electron influences the outer electron and the resulting correlation effects can be detected in energy shifts conveniently parameterized in terms of quantum defects [21,22]. The autoionizing states for high- ℓ levels have been frequently analyzed using a perturbative approach [23,35,36] by considering the weak electron-electron interaction as the perturbation. For low ℓ , where the Rydberg electron penetrates the inner valence electron, the perturbative approach breaks down and the multichannel quantum defect theory [37] can be used to analyze the autoionizing levels.

Here we present a comprehensive study, using both theory and experiment, of $^{88}\text{Sr } 5p_{1/2}n\ell_j$ autoionizing Rydberg states. Experimentally determined lifetimes and quantum defects of the autoionizing states are compared with theoretical nonperturbative solutions of this quasi-two-electron problem employing the exterior complex rotation (ECR) method [16,22,38]. This method of calculating atomic resonances in the complex plane allows the discrimination of quasibound autoionizing levels from scattering states using square-integrable wave functions. We examine, in particular, the ℓ dependence of the autoionization rates. While the latter is expected to follow the ℓ^{-5} scaling derived from the perturbation theory, the deviations from this scaling law at low ℓ help elucidate the effects of exchange interactions and intruder states. For states with $n \leq 60$, a direct state-resolved comparison between our theoretical predictions and earlier measurements is possible. For a comparison with new measurements for very high n ($120 \lesssim n \lesssim 200$) we apply an extrapolation of our ECR results for low n to predict autoionization rates. These high-lying autoionizing states are prepared by exciting first a singly excited Rydberg state $5sn\ell$ followed by excitation of the $5s_{1/2} \rightarrow 5p_{1/2}$ transition in the core ion (see Fig. 1). In the high n limit, typically, the intruder states are absent and the scaling with respect to n and ℓ can be extracted with small uncertainties. While several autoionizing resonances can overlap due to the high density of states, the calculated autoionization rates, energy shifts, and oscillator strengths reproduce well the measured excitation profiles.

The structure of the paper is as follows. In Sec. II we briefly review our present experimental approach. The properties of lower-lying autoionizing Rydberg states of Sr ($n \leq 60$) and their theoretical description are presented in Sec. III. The application to atom loss spectra for high-lying autoionizing Rydberg states with $n \geq 120$ is discussed in Sec. IV followed by concluding remarks (Sec. V).

II. EXPERIMENTAL APPROACH

In the present work autoionization is explored through studies of Rydberg atom loss induced by excitation of the 422-nm $5s^2S_{1/2} \rightarrow 5p^2P_{1/2}$ transition in the Sr^+ core ion.

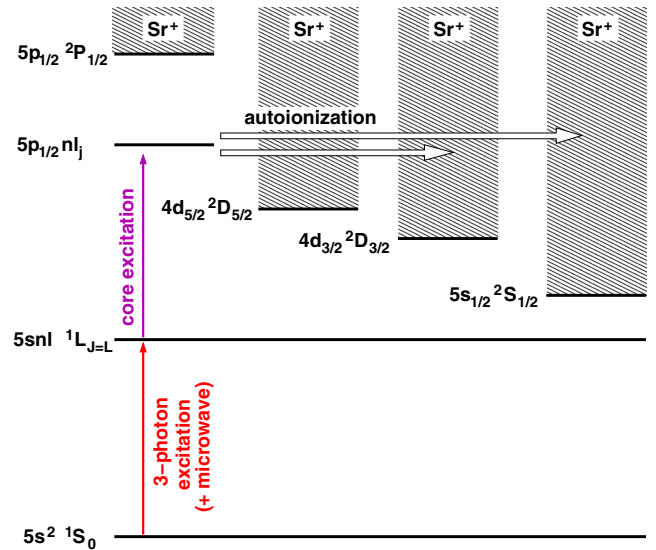


FIG. 1. Schematic energy-level diagram for autoionization of doubly excited strontium Rydberg states near the Sr^+ ionization threshold. Initially, the ground-state atom is excited to a singly excited $5sn\ell \ ^1L_J$ Rydberg state by three-photon excitation (in some cases with an additional microwave field). The second valence electron is then excited to create doubly excited $5p_{1/2}n\ell_j$ states. These autoionize predominantly to $5s_{1/2}\ell'_j$ or $4d_{3/2}\ell'_j$ levels. The state of the second valence electron for each Sr^+ threshold is indicated.

Measurements focus on the fractional loss of Rydberg atoms due to autoionization which is determined through alternating measurements of the number of Rydberg atoms created and the number that remain following exposure to the 422-nm radiation. Autoionization loss spectra are obtained by recording the fractional loss as the 422-nm laser is scanned across the core ion transition. Initial Rydberg states with $120 \lesssim n \lesssim 200$ are selected for study because, for such states, decay due to autoionization is more rapid than that due to radiative decay of the inner valence electron, whereupon the loss of Rydberg atoms can be identified as a measure of the autoionization rate. Autoionization loss profiles recorded using several different values of n and a given ℓ are used to extract the n scaling of the autoionization rates, and the quantum defects.

A schematic diagram of the present apparatus, component parts of which are described in detail elsewhere [16], is shown in Fig. 2. Briefly, strontium atoms contained in a collimated beam are excited to the selected high- n $5sn\ell$ state by multiphoton excitation near the center of an interaction region defined by three pairs of copper electrodes. $5snp \ ^1P_1$ and $5snf \ ^1F_3$ states are created by the three-photon excitation schemes shown in Fig. 2 that utilize the $5s5p \ ^1P_1$ and $5s5d \ ^1D_2$ intermediate states. The required radiation at 461, 767, and 893 nm is provided by diode laser systems. All three laser beams are polarized along the x axis resulting in the creation of states with $|M_J| = 1$ (and 3). Other ℓ levels ($5sns$, $5snd$, $5sng$, and $5snh$) are created by multiphoton optical and microwave excitation (see Fig. 2). The 893-nm laser is first detuned by ~ 45 –60 MHz from the transition to a $5snp \ ^1P_1$ or $5snf \ ^1F_3$ state which is sufficient to suppress any significant direct excitation of either state. Rydberg production is then recovered by the simultaneous addition of a microwave field

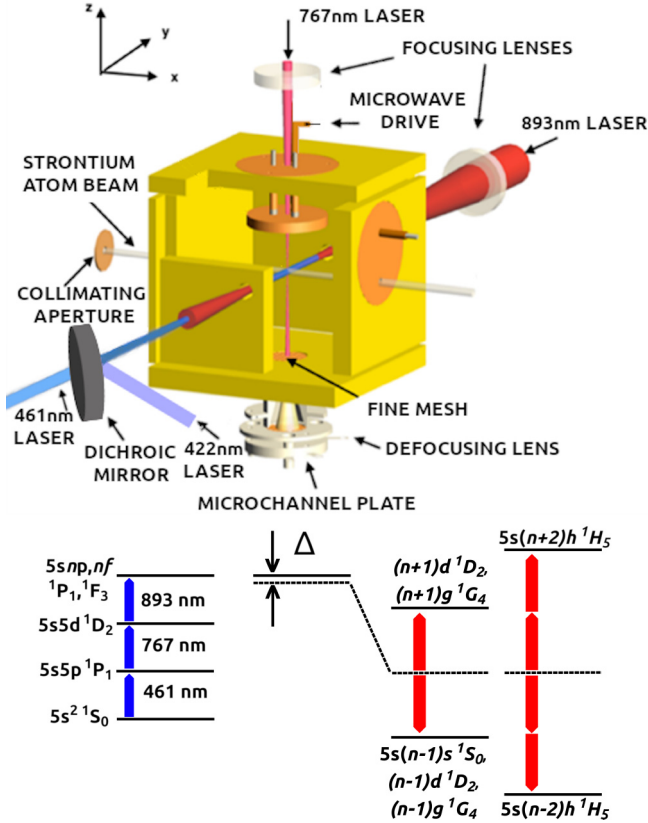


FIG. 2. Schematic diagram of the present apparatus. The schemes employed to create the different $5sn\ell$ states are also shown where blue (red) arrows denote optical (microwave) photons.

tuned to allow direct combined four- or five-photon optical and microwave excitation of the desired state. The microwave radiation is generated by applying the output of a frequency synthesizer to a circular electrode positioned above the excitation volume. The amplitudes of the microwave drive voltages are typically rather small, $\lesssim 20$ mV. Ancillary studies show that application of a DC bias of 20 mV to the electrode results in the Rydberg atoms experiencing a DC field of ~ 3 mV cm^{-1} . Here we use microwave frequencies of $\sim 2\text{--}4$ GHz. Because of retardation effects it is not possible to directly relate the amplitude of the microwave drive voltage to the microwave field generated in the excitation region. Furthermore, because of possible internal reflections the polarization of the microwave field is not well defined leading to ambiguity in the distribution of final $|M_J|$ states populated. However, it is reasonable to expect that, for a given drive frequency, the amplitude of the microwave field will be proportional to the drive voltage.

Experiments are conducted in a pulsed mode. The output of the 461-nm laser and (if required) frequency synthesizer are chopped into a series of simultaneous pulses of ~ 1 μs duration with a pulse repetition frequency of ~ 10 kHz (the other two laser beams remain on at all times). After a brief (~ 200 ns) delay autoionization can be induced by exciting the $5s\ ^2S_{1/2} \rightarrow 5p\ ^2P_{1/2}$ transition in the Sr^+ ion using a $1\mu\text{s}$ -long pulse of 422-nm radiation polarized along the z axis that is generated by a diode laser system whose

output frequency is referenced to the $5s\ ^2S_{1/2}(F' = 2) \rightarrow 5p\ ^2P_{1/2}(F' = 3)$ transition in ^{85}Rb which lies 440 MHz to the red of the core ion transition [39]. After a brief time delay to allow electrons produced by autoionization to be lost to the walls, the number of surviving Rydberg atoms is determined by selective field ionization (SFI) [40,41]. An increasing electric field is produced in the experimental volume by applying a linearly increasing positive voltage ramp (rise time ~ 4 μs) to the lower electrode. The product electrons are collected and detected using a dual microchannel plate. The probability that a Rydberg atom is created during any experimental cycle is small, $\lesssim 0.6$, and data are accumulated over many cycles to build up good statistics. The fractional loss of Rydberg atoms due to autoionization is determined through measurements of the Rydberg atom signal with and without the 422-nm laser pulse applied.

Before analyzing the measured autoionization profiles, we look at the properties of autoionizing states. In particular, the autoionization rates, the quantum defects, and the oscillator strengths of autoionizing states are examined since they are necessary information to simulate the excitation dynamics.

III. PROPERTIES OF AUTOIONIZING STATES

The autoionization of quasi-two-electron systems, such as strontium, can be numerically analyzed using the two-active-electron approximation [42]. Denoting the Sr^{2+} ion core potential with $V_c(r)$ the Hamiltonian of the two-valence-electron system can be written as

$$H = \sum_{i=1}^2 \left(\frac{p_i^2}{2} + V_c(r_i) + V_{\text{so}}(r_i) \right) + V_{ee}, \quad (1)$$

where \vec{p}_i and $\vec{r}_i (i = 1, 2)$ are the momenta and positions of the two valence electrons (atomic units are used throughout unless otherwise noted). The electron-electron interaction is denoted by

$$V_{ee} = \frac{1}{|\vec{r}_1 - \vec{r}_2|} \quad (2)$$

and the spin-orbit interaction is given by

$$V_{\text{so}}(r) = \frac{\alpha^2}{2} (\vec{\ell} \cdot \vec{s}) \frac{1}{r} \frac{dV_c(r)}{dr}, \quad (3)$$

where α is the fine-structure constant. In strontium, the spin-orbit coupling is relatively large giving rise to a fine-structure splitting between the $5p_{1/2}$ and $5p_{3/2}$ levels in the Sr^+ ion of $\sim 3.7 \times 10^{-3}$ a.u. (or ~ 0.1 eV). For high Rydberg states with $n \gg 1$ the electron-electron interaction V_{ee} is strongly reduced for $5pn\ell$ autoionizing states and, therefore, is often treated as a perturbation. We first briefly review the well-known perturbative treatment for autoionization of these states (see, e.g., [23,35,36]) which will serve as point of reference for our present nonperturbative simulations. This will aid in understanding both the measured data and numerical results presented in the later sections.

A. Perturbative approach

In the perturbative treatment the electron-electron interaction V_{ee} is considered as a perturbation and expanded in

multipole terms, i.e.,

$$V_{ee} = \sum_{k=0}^{\infty} U_k(\vec{r}_1, \vec{r}_2), \quad (4)$$

with

$$U_k(\vec{r}_1, \vec{r}_2) = \sum_{m_k=-k}^k \left[\frac{r_{<}^k}{r_{>}^{k+1}} \frac{4\pi}{2k+1} Y_k^{m_k}(\Omega_1) Y_k^{m_k*}(\Omega_2) \right], \quad (5)$$

where $r_{>}$ ($r_{<}$) indicates the larger (smaller) between r_1 and r_2 and Ω_i ($i = 1, 2$) the solid angle of the i th electron. The ‘‘unperturbed’’ Hamiltonian, defined as

$$H_0 = \sum_{i=1}^2 \left(\frac{p_i^2}{2} + V_c(r_i) + V_{so}(r_i) \right) + U_0(\vec{r}_1, \vec{r}_2), \quad (6)$$

includes the zeroth-order multipole (or screening) term $U_0(\vec{r}_1, \vec{r}_2) = 1/r_{>}$ of the core potential by the inner valence electron while the higher multipoles U_k ($k \geq 1$) represent the perturbation. H_0 is diagonalized using the (nonantisymmetrized) basis states given in coordinate representation as

$$\begin{aligned} & \langle \vec{r}_1, \vec{r}_2 | (n_v, \ell_{j_v}, n, \ell_j) J \rangle_0 \\ &= \frac{\psi_{n_v, \ell_{j_v}}(r_1) F_{n, \ell_j}(r_2)}{r_1} \langle \Omega_1, \Omega_2 | (\ell_{j_v}, \ell_j) J \rangle, \end{aligned} \quad (7)$$

where n is the principal quantum number and ℓ the orbital angular momentum of the Rydberg electron. $\psi_{n_v, \ell_{j_v}}$ and F_{n, ℓ_j} are the radial wave function of the inner valence electron (with subindex v) and of the Rydberg electron, respectively. The total angular momentum of each electron is $\vec{j}_{(v)} = \vec{\ell}_{(v)} + \vec{s}_{(v)}$ and the total angular momentum $\vec{J} = \vec{j}_v + \vec{j}$. The radial wave functions satisfy the eigenvalue equations

$$\left[-\frac{1}{2} \partial_{r_v}^2 + V_c(r_v) + V_{so}(r_v) \right] \psi_{n_v, \ell_{j_v}}(r_v) = I_{n_v, \ell_{j_v}} \psi_{n_v, \ell_{j_v}}(r_v), \quad (8)$$

and

$$\left[-\frac{1}{2} \partial_r^2 + V_{\text{eff}}(r) + V_{so}(r) \right] F_{n, \ell_j}(r) = E_{n, \ell_j}^{(0)} F_{n, \ell_j}(r), \quad (9)$$

with the effective core potential

$$\begin{aligned} V_{\text{eff}}(r) &= V_c(r) + \int_0^r dr_v |\psi_{n_v, \ell_v}(r_v)|^2 \\ &+ \int_r^\infty dr_v \frac{1}{r_v} |\psi_{n_v, \ell_v}(r_v)|^2. \end{aligned} \quad (10)$$

For two valence electrons outside a closed-shell core, the two-electron basis states should be antisymmetrized, i.e.,

$$\begin{aligned} |(n_v, \ell_{j_v}, n, \ell_j) J \rangle_A &= \frac{1}{\sqrt{2}} \left[|(n_v, \ell_{j_v}, n, \ell_j) J \rangle_0 \right. \\ &\left. - (-1)^{j_v+j+J} |(n, \ell_j, n_v, \ell_{j_v}) J \rangle_0 \right]. \end{aligned} \quad (11)$$

As a result of antisymmetrization, wave functions belonging to different two-electron configurations, e.g., $5s_{1/2}n p_j$ and $5p_j n s_{1/2}$, are no longer orthogonal to each other. Therefore, when the radial equation for the Rydberg electron is solved for each two-electron configuration, the Hamiltonian matrix is diagonalized in a subspace of the Hilbert space orthogonal

to all other configurations to maintain the orthogonality in the antisymmetrized basis.

The autoionization rate follows now in first-order approximation from the Wentzel-Fermi golden rule [23,36,43,44] as

$$\Gamma = 2\pi \sum_{n'_v, \ell'_v, j'_v, \ell'_j} |A_d - (-1)^{j_v+j+J} A_{\text{ex}}|^2, \quad (12)$$

and the energy shift as

$$\Delta E^{(2)} = \sum_{n'_v, \ell'_v, j'_v, \ell'_j} \mathcal{P} \int d\epsilon \frac{|A_d - (-1)^{j_v+j+J} A_{\text{ex}}|^2}{I_{n_v, \ell_{j_v}} - I_{n'_v, \ell'_{j_v}} + E_{n, \ell_j}^{(0)} - \epsilon}, \quad (13)$$

where \mathcal{P} indicates the principal value. The direct and exchange amplitudes are defined as

$$A_d = \sum_{k=1}^{\infty} \langle (n'_v, \ell'_{j_v}, \epsilon, \ell'_j) J | U_k | (n_v, \ell_{j_v}, n, \ell_j) J \rangle_0, \quad (14)$$

and

$$A_{\text{ex}} = \sum_{k=0}^{\infty} \langle (\epsilon, \ell'_j, n'_v, \ell'_{j_v}) J | U_k | (n_v, \ell_{j_v}, n, \ell_j) J \rangle_0, \quad (15)$$

where $|(n'_v, \ell'_{j_v}, \epsilon, \ell'_j) J\rangle$ is a continuum state lying energetically above the ionization threshold $I_{n'_v, \ell'_{j_v}}$. The evaluation of the direct and exchange amplitudes employs the numerically evaluated bound and continuum radial wave functions, which account for the phase shift induced by the effective core potential [Eq. (10)]. The continuum state in Eq. (12) satisfies the resonance condition $I_{n'_v, \ell'_{j_v}} + \epsilon \simeq I_{n_v, \ell_{j_v}} + E_{n, \ell_j}^{(0)}$. In Eq. (13) the integral over energy includes not only the continuum states but also the bound states. The exchange amplitude is nonvanishing when the selection rule $\ell \leq \ell'_v + k$ is satisfied. For the $5p_{1/2}n\ell$ autoionizing states of strontium, the inner valence electron decays from the $5p$ to the $5s$ or $4d$ state (Fig. 1) and couples predominantly to the neighboring $5s$, $4d$, $6s$, and $5d$ states (i.e., $\ell'_v \leq 2$). The leading terms in Eqs. (14) and (15) are therefore $k = 1$ for the direct term and $k = 0, 1$ for the exchange. Consequently, the exchange interaction contributes significantly only for $\ell \leq 3$. Moreover, the radial wave function of the Rydberg electron, $F_{n, \ell_j}(r)$, with $\ell \geq 4$ barely overlaps with the inner valence wave function, $\psi_{n'_v, \ell'_{j_v}}(r)$, with $\ell'_v \leq 2$ suppressing the exchange amplitude for $\ell \geq 4$. Thus, for large angular momentum states with $\ell \geq 4$ the energy shift can be simplified [20,45] to

$$\Delta E^{(2)} \simeq -\frac{1}{2} \alpha_d \langle n, \ell | r^{-4} | n, \ell \rangle, \quad (16)$$

where α_d is the effective dipolar polarizability of the excited Sr^+ ion core and where it is assumed that the dominant contributions to the integral [Eq. (13)] originate from the states with transition frequencies of the outer electron small compared to that of the inner electron, i.e., $|\epsilon - E_{n, \ell_j}^{(0)}| \ll |I_{n_v, \ell_{j_v}} - I_{n'_v, \ell'_{j_v}}|$. The effective polarizability accounts for the relative angles between the induced dipoles of the inner valence and the Rydberg electrons [see Eq. (5) with $k = 1$] and therefore depends not only on the state of the inner electron, but also on the angular momentum of the Rydberg electron. The quantum defect of the high- ℓ autoionizing states can thus be evaluated

as

$$\mu = \mu^{(0)} + \mu^{(2)}, \quad (17)$$

where the zeroth-order correction is given by $E_{n,\ell_j}^{(0)} = -1/[2(n - \mu^{(0)})^2] \simeq -1/(2n^2) - \mu^{(0)}/n^3$ and the second-order correction is

$$\begin{aligned} \mu^{(2)} &= -n^3 \Delta E^{(2)} \\ &\simeq \frac{3\alpha_d}{4(\ell + 3/2)(\ell + 1)(\ell + 1/2)\ell(\ell - 1/2)}. \end{aligned} \quad (18)$$

In Eq. (18) the expectation value $\langle n, \ell | r^{-4} | n, \ell \rangle$ is evaluated using hydrogenic wave functions in the limit of large n . The static polarizability of the 5P_{1/2} ²P_{1/2} strontium ion is estimated to be $\alpha_d = -49$ [46,47]. This negative polarizability may affect the sign of the quantum defect [Eq. (17)] for large ℓ . For two-electron atoms, the transition energy $|\epsilon - E_{n,\ell_j}^{(0)}|$ of the Rydberg electron in Eq. (13) may not be negligible compared to that of the inner valence electron, $|I_{n_v, \ell_{jv0}} - I_{n_v, \ell'_{jv0}}|$, and the approximation [Eq. (16)] to the energy shift may break down requiring a more accurate estimate [35].

For Rydberg states with small angular momenta, $\ell < 4$, the evaluation of autoionization rates [Eq. (12)] and energy shifts [Eq. (13)] is more involved due to the nonnegligible contributions from the exchange amplitude [Eq. (15)]. The exchange interaction [Eq. (15)] can also lead to sizable couplings between the autoionizing states, 5P_{1/2}ns_j and 5P_{1/2}nd_j, as well as between the 5P_{1/2}nℓ_j state and the intruder 5P_{3/2}nℓ_j state. Such couplings are neglected in the perturbative approach. In the next section, we compare the estimates from perturbation theory [Eq. (12)] with numerical nonperturbative calculations.

B. Nonperturbative quasi-two-electron approximation

The autoionization rate of the 5P_{1/2}nℓ_j autoionizing states is evaluated using an *ab initio* calculation by numerically diagonalizing the Hamiltonian [Eq. (1)]. The Hilbert subspace is defined by limiting the inner valence electron configurations to 5s_{1/2}, 4d_{j_v}, 5p_{j_v}, 6s_{1/2}, 5d_{j_v}, and 6p_{j_v}. This limits also the number of contributing multipole terms U_k , all of which are included in the calculation. For the evaluation of autoionization rates, we employ the exterior complex rotation (ECR) method [16,38]. While the radial wave function of the outer electron is evaluated within a finite region of coordinate space, an outgoing boundary condition (instead of hard wall) is enforced at the boundary. Scattering states feature, typically, large loss rates due to this imposed outgoing boundary condition. On the other hand, autoionizing states are quasibound and couple only weakly to scattering states. Consequently, the loss rates for autoionizing states become nearly independent of the outgoing boundary condition. Thus, in the ECR method, the autoionizing states can be distinguished from nearby scattering states by their insensitivity to the variation of the outgoing boundary condition. Moreover, they, typically, feature much smaller imaginary parts of the eigenenergies than a scattering state which allows the extraction of autoionization rates. Correspondingly, the energy shifts of the autoionizing states can be extracted from the real part of the eigenenergy. In our simulations the converged autoionization rates and eigenenergies can be obtained for n states up to

TABLE I. Parameters for the model potential [Eq. (19)].

ℓ	a_1	a_2	a_3	r_c	α_{cp}
0	3.01	1.00	1.07	3.00	
1	3.15	0.89	1.21	1.38	
2	4.20	1.59	1.12	0.62	5.3
≥ 3	4.81	4.07	1.76	0.95	

$n \sim 60$. They are extrapolated to higher n for a comparison with the new measurements in the high- n ($n > 120$) limit. In this regime, several resonances are overlapping and cannot be resolved experimentally. The application of the ECR method is particularly convenient as it does not require any fitting to state-resolved autoionization spectra as needed in multichannel quantum defect theory. In our simulation we employ the core potential representing the closed-shell Sr²⁺ core [Eq. (1)]

$$V_c(r) = -\frac{1}{r} \left(1 + 37e^{-a_1 r} + a_2 e^{-a_3 r} - \frac{\alpha_{cp}}{2r^4} (1 - e^{-(r/r_c)^6}) \right), \quad (19)$$

which includes the effects of the static dipolar polarizability α_{cp} of the Sr²⁺ ion (see the parameters in Table I). The potential has been optimized to obtain the quantum defects for singly excited states with deviations of < 0.01 . This error implies deviations in energy of $< 0.01/n^3$. While small on an absolute scale, it may result in errors on the scale of the fine-structure splitting. For example, the measured fine-structure splitting of the 5p state of Sr⁺ ion is 3.65×10^{-3} a.u. while the model potential yields 3.99×10^{-3} . Therefore, the effect of intruder states (5P_{3/2}nℓ_j) on the 5P_{1/2}nℓ_j autoionizing states cannot be accurately described. However, in the absence of such intruder states at large n , autoionization rates and energy shifts have well converged. We have verified convergence by additional calculations using different core potentials that yield slightly different Sr⁺ energies and shifts in the position of the intruder states. In the following, autoionization rates calculated using ECR will be compared to those obtained using the perturbative approach [Eqs. (12) and (13)]. The latter can also serve as a benchmark for spectra in the absence of intruder states and configuration mixing. The perturbative approach can be easily applied to autoionizing states with values of n up to $\simeq 200$ while the ECR method is limited to states with $n < 60$. We therefore employ perturbation theory to extrapolate *ab initio* results to higher n , as discussed below.

Figure 3 shows autoionization rates for the 5P_{1/2}ns_{1/2} ($J = 1$) states calculated by both the ECR method (triangles) and perturbation theory (PT, solid line) [Eq. (12)]. The effective quantum number $\nu_{5P_{1/2}}$ is defined with respect to the ionization threshold $I_{5P_{1/2}}$ associated with the Sr⁺ ion state 5P_{1/2} ²P_{1/2}, i.e., $\nu_{5P_{1/2}} = [2(I_{5P_{1/2}} - E)]^{-1/2}$, where E is the energy of the autoionizing state. In the perturbative approach $\nu_{5P_{1/2}}$ is evaluated using the unperturbed energy $E = E_{ns_{1/2}}^{(0)}$ [Eq. (9)]. For comparison the experimental data (circles) from Ref. [31] are also included in Fig. 3. The ECR results show strongly fluctuating autoionization rates where the “peaks” result from the coupling to 5P_{3/2}ns_{1/2} ($J = 1$) intruder states. The coupling to these intruder states tends to increase the autoionization rate Γ . The positions of these peaks are slightly

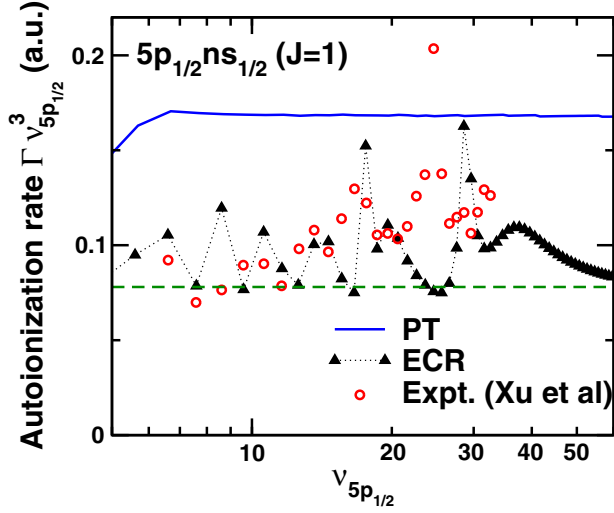


FIG. 3. Autoionization rates of $5p_{1/2}ns_{1/2}(J=1)$ states calculated by the ECR method (triangles) and by perturbation theory (PT, solid line) [Eq. (12)]. The effective quantum number $\nu_{5p_{1/2}}$ is defined with respect to the ionization threshold $I_{5p_{1/2}}$. The autoionization rate is scaled by a factor of $\nu_{5p_{1/2}}^3$. The open circles are the measured data from [31] and the dashed lines show the value of Γ_0 obtained by fitting the ECR results [see text, Eq. (20)]. The results from the ECR method are connected by dotted lines to visualize the peak positions.

shifted relative to those in the experimental data because of the discrepancy in the fine-structure splitting of the $5p$ Sr^+ ion state discussed above. The autoionization rates calculated using the ECR method are fit to a power-law scaling

$$\Gamma \simeq \Gamma_0 \nu_{5p_{1/2}}^{-3} \quad (20)$$

(see the dashed line in Fig. 3) where Γ_0 is determined from the intruder-free region at large values of the effective quantum number $\nu_{5p_{1/2}}$ (in the present case $\nu_{5p_{1/2}} > 50$). Correspondingly, Eq. (20) provides a lower bound to the autoionization rates Γ for smaller values of $\nu_{5p_{1/2}}$, consistent with the enhancement of Γ by the presence of intruder states. We note that the present fitting procedure differs from that employed in [16] where Γ was determined by a least-squares deviation fit to all data rather than to the data in the intruder-free region. Therefore, the values of Γ extracted from the current fit are slightly smaller (see Table II). The perturbative approach also shows a $\nu_{5p_{1/2}}^{-3}$ scaling but consistently overestimates the autoionization rate. The discrepancy between the values of Γ derived using perturbation theory and ECR results primarily from the non-negligible admixture (1–5%) of the configuration $|5p_{1/2}nd_{3/2}, J=1\rangle_0$. Similar interactions between different configurations were observed for small $\nu_{5p_{1/2}}$ [31].

For the $5p_{1/2}np_j$ autoionizing states (see Fig. 4), the measured data (circles) and the ECR calculations (triangles) agree well with each other. Again the perturbative approach (solid line) yields results that deviate from both of these. These deviations originate from the mixing between the bound configurations ($5p_i np_j$) induced by the exchange interaction of the $U_{k=0}$ term [Eq. (15)] and by the higher multipole term $U_{k=2}$. The fitted value of Γ_0 [Eq. (20)] to the ECR

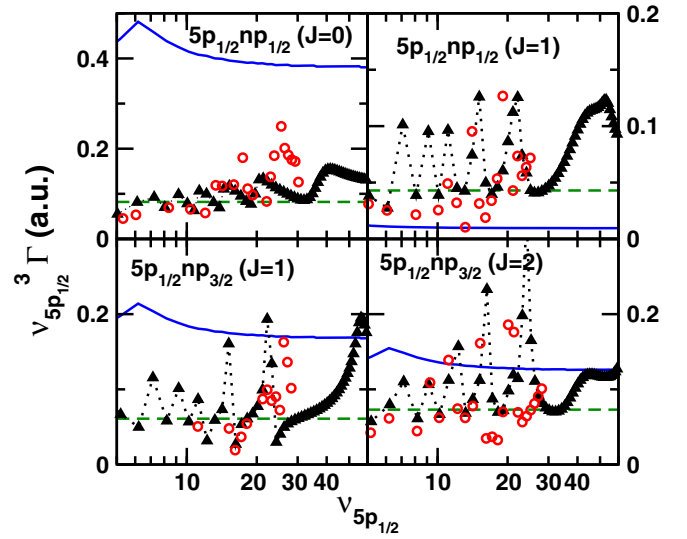


FIG. 4. Autoionization rates of $5p_{1/2}np_j$ states calculated by the ECR method (triangles) and by perturbation theory (PT, solid line) [Eq. (12)]. The open circles are the measured data from [33] and the dashed lines show the value of Γ_0 obtained by fitting the ECR results [Eq. (20)].

results can be found in Table II. For $\ell = 1$, intruder states ($5p_{3/2}np_j$) are present around $\nu_{5p_{1/2}} \simeq 50$ and Γ_0 is obtained by fitting to the lower bound of the (fluctuating) Γ . As is the case for $\ell = 0$ states (see Fig. 3), the positions of peaks caused by the intruder states ($5p_{3/2}np_j$) are shifted relative to the measured data but the overall magnitudes of Γ agree reasonably well.

With further increases in ℓ , the mixing of configurations is suppressed and the ECR and perturbative calculations move into agreement. (The fitted values of Γ_0 for other values of ℓ are also listed in Table II.) For example, for the $5p_{1/2}ng_j$ states (Fig. 5), the two calculations of Γ agree reasonably well except for the effects of intruder states. The narrow width of the peaks induced by intruder states indicate that the mixing between the intruder state and the nearby autoionizing state is weak for large ℓ . In this high- n , high- ℓ limit, the spin of the Rydberg electron becomes less important and the autoionizing states are often represented by the intermediate coupling scheme using the quantum number $\vec{K} = \vec{j}_v + \vec{\ell}$. States with the same quantum number K become degenerate regardless of j values. Indeed, the transformation between the jj and intermediate representations [48] for $J = \ell$ is

$$\begin{aligned} \begin{pmatrix} |(p_{1/2} \ell_{j=\ell-1/2}) J \rangle_0 \\ |(p_{1/2} \ell_{j=\ell+1/2}) J \rangle_0 \end{pmatrix} &= \begin{pmatrix} \cos \theta & -\sin \theta \\ \sin \theta & \cos \theta \end{pmatrix} \\ &\times \begin{pmatrix} |((p_{1/2} \ell) K = \ell + 1/2, s) J \rangle_0 \\ |((p_{1/2} \ell) K = \ell - 1/2, s) J \rangle_0 \end{pmatrix}, \end{aligned} \quad (21)$$

with $\theta = \arctan[1/(2\sqrt{J(J+1)})]$. In the limit of large J , or equivalently, of large ℓ , the mixing angle θ vanishes and two representations become identical. States with $(j, J) = (\ell - 1/2, \ell)$ and $(\ell + 1/2, \ell + 1)$ having $K = \ell + 1/2$ become degenerate and so do the states with $(j, J) = (\ell + 1/2, \ell)$ and

TABLE II. Fitted values of the scaled autoionization rate Γ_0 [see Eq. (20)] and the scaled line center shifts, Δ_L [see Eq. (22)] together with the fractional part of the quantum defect $\mu_{5p_{1/2}} = \lceil v_{5p_{1/2}} \rceil - v_{5p_{1/2}}$ where $v_{5p_{1/2}}$ is the effective quantum number with respect to the ionization threshold $I_{5p_{1/2}}$. Values from new measurements are discussed in Sec. IV. Values derived from earlier studies at higher n [16] are included and indicated by an asterisk. (In this earlier work the $np_{1/2}$ and $np_{3/2}$ features could not be resolved, resulting in a broader overall linewidth.) For $\ell = 2$, the line centers for both the features at positive and negative detunings are indicated. Γ_0 and $\mu_{5p_{1/2}}$ are approximately equal for both features.

State	$\Gamma_0 / (2\pi)$			$\Delta_L v_{5s}^3$	Quantum defect, $\mu_{5p_{1/2}}$			
	Expt. (MHz)	Expt. (a.u.)	Calc. (a.u.)		Expt. (a.u.)	Calc. (a.u.)		
5p _{1/2} ns _{1/2} (J = 1)	5.2 × 10 ⁸	0.079	0.078	−8.0 × 10 ⁸	0.39	0.394		
5p _{1/2} np _{1/2} (J = 0)	-	-	0.082	-	-	0.78		
5p _{1/2} np _{1/2} (J = 1)	-	-	0.043	−1.4 × 10 ⁹	0.94	0.92		
5p _{1/2} np _{3/2} (J = 1)	3.3 × 10 ⁸	0.050	0.061	−7.2 × 10 ⁸	0.84	0.815		
5p _{1/2} np _{3/2} (J = 2)	(5.0 × 10 ⁸ *)	(0.076*)	0.073	(−7.3 × 10 ⁸ *)	(0.84*)	0.83		
5p _{1/2} nd _{3/2} (J = 1)			0.378			0.74		
5p _{1/2} nd _{3/2} (J = 2)	7.1 × 10 ⁸	0.108	0.096	−2.4 × 10 ⁹	0.74	0.81		
5p _{1/2} nd _{5/2} (J = 2)			0.230	3.7 × 10 ⁹		-	0.70	
5p _{1/2} nd _{5/2} (J = 3)			0.128			0.76		
5p _{1/2} nf _{5/2} (J = 2)					0.199			0.12
5p _{1/2} nf _{5/2} (J = 3)	1.19 × 10 ⁹	0.181	0.164	−2.8 × 10 ⁸	0.13	0.1		
5p _{1/2} nf _{7/2} (J = 3)	(1.34 × 10 ⁹ *)	(0.204*)	0.201	(−3.0 × 10 ⁸ *)		(0.13*)	0.13	
5p _{1/2} nf _{7/2} (J = 4)			0.230				0.05	
5p _{1/2} ng _{7/2} (J = 3)			0.081			0.996		
5p _{1/2} ng _{9/2} (J = 4)	3.7 × 10 ⁸	0.056		0.046	1.8 × 10 ⁸		0.01	0.993
5p _{1/2} ng _{7/2} (J = 4)								
5p _{1/2} ng _{9/2} (J = 5)								
5p _{1/2} nh _{9/2} (J = 4)			0.015			0.991		
5p _{1/2} nh _{11/2} (J = 5)	1.8 × 10 ⁸	0.027		0.7 × 10 ⁸	0.002			
5p _{1/2} nh _{9/2} (J = 5)						0.006		
5p _{1/2} nh _{11/2} (J = 6)								

($\ell - 1/2, \ell - 1$) with $K = \ell - 1/2$. The real parts of the complex energy eigenvalues resulting from the ECR calculation, parameterized in terms of quantum defect μ , can be compared with the measured data [31–33] as well (Fig. 6). The quantum defect $\mu_{5p_{1/2}}$ is defined as $\mu_{5p_{1/2}} = \lceil v_{5p_{1/2}} \rceil - v_{5p_{1/2}}$ with the ceiling function $\lceil \cdot \rceil$. Similar to Γ , the effects of intruder states are clearly seen. While the exact positions of the intruder states in the calculation are again slightly shifted as compared to the experimental data, their overall behavior appears to agree well. For most states, the asymptotic value of the quantum defect in the large $v_{5p_{1/2}}$ limit can be extracted from the calculations near $v_{5p_{1/2}} \simeq 60$ (Fig. 6). For the 5p_{1/2}np_j, $J = 1$ states, however, deviations due to intruder states are present around $v_{5p_{1/2}} \simeq 50$ –60. Therefore, the asymptotic value is, instead, fit to the region where the autoionizing states have only a small admixture of $[5p_{3/2}n\ell_j]_0$ configurations.

Due to the singularity present in the integrand [Eq. (13)] it is challenging to obtain converged energy shifts from the perturbative approach. Only for large ℓ , does the exchange amplitude become negligible allowing the approximation

[Eq. (16)] to be applied. The quantum defect due to the ion core screened by the 5p_{1/2} inner valence electron is $\mu^{(0)} \simeq 0.0033$ for $\ell = 4$ and 0.00085 for $\ell = 5$. The additional correction due to the electron-electron interaction [Eq. (17)] derived using the polarizability $\alpha_d = -49$ [46] is $\mu^{(2)} \simeq -0.021$ for $\ell = 4$ and -0.0076 for $\ell = 5$. The resulting total quantum defects (modulo 1) within perturbative theory are $\mu_{5p_{1/2}} = 0.982$ for $\ell = 4$ and 0.993 for $\ell = 5$, as shown in Fig. 7. The corresponding results from the ECR calculation agree with perturbation theory in regions well removed from the spectral positions of the intruder states to within an error of about 0.01. However, near $v_{5p_{1/2}} \simeq 40$ the distortion introduced by the intruder state, which is included in the ECR calculation, but is absent in the perturbation theory, leads to significant discrepancies. In turn, the asymptotic value of $\mu_{5p_{1/2}}$ (Table II) is extrapolated by fitting the Rydberg-Ritz formula to the ECR results in the intruder-free region around $v_{5p_{1/2}} > 55$. The perturbative approximation [Eq. (16)] assumes that the inner and outer valence electrons are uncorrelated and, therefore, the resulting energy shift does not depend on $K = \ell \pm 1/2$. To remove the degeneracy within

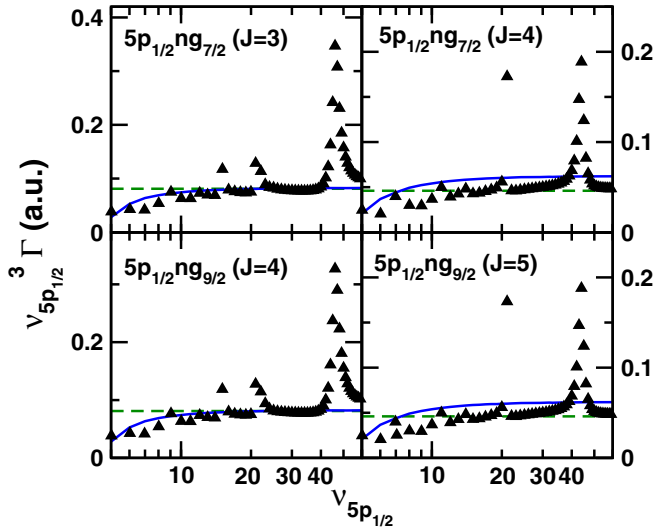


FIG. 5. Autoionization rates for $5p_{1/2}ng_j$ states calculated by the ECR method (triangles) and by perturbation theory (PT, solid line) [Eq. (12)]. The dashed lines show the values of Γ_0 obtained from a fit to the ECR results.

PT, a more accurate estimate [Eq. (13)] would be required by taking the energy difference in unperturbed energy $E_{n,\ell_j}^{(0)}$ between different K levels.

IV. RYDBERG ATOM LOSS SPECTRA

In this section, we compare the theoretical predictions discussed above with the new measurements of autoionizing states for $120 \lesssim n \lesssim 200$. The calculated autoionization rates for $n < 60$ are extrapolated to the high- n levels following the $\Gamma = \Gamma_0 v_{5p_{1/2}}^{-3}$ scaling. The quantum defects fitted to the ECR results are assumed to be the asymptotic value and valid for the measured data for $n > 120$. Different from the autoionizing states for low n , several autoionizing resonances overlap and cannot often be resolved due to the high density of states. Therefore, the information on each individual autoionizing state cannot be extracted and the comparison between the measurements and the calculations need to be done differently. We simulate the excitation dynamics using the calculated Γ_0 and $\mu_{5p_{1/2}}$ and, also, the numerically evaluated oscillator strengths. The resulting excitation profiles can be tested against the measured data.

Autoionization loss profiles recorded using $5sns \ ^1S_0$ Rydberg atoms are presented in Fig. 8. To facilitate a visual comparison of the different profiles, the 422-nm laser power was adjusted to achieve similar peak losses of $\sim 30\text{--}35\%$ in each profile. Considering that direct photoionization from the singly excited state is negligible, an autoionizing state can be considered to represent a Breit-Wigner resonance with a Lorentzian profile. The red solid lines in Fig. 8 are Lorentzian fits to the measurements. The line center is associated with the quantum defect $\mu_{5p_{1/2}}$ and the width with the autoionization rate Γ . To correct for saturation near the line center and for ac Stark shifts, for each value of n loss profiles were measured for several values of 422-nm laser power and the results extrapolated to zero laser power. The resulting widths, together with

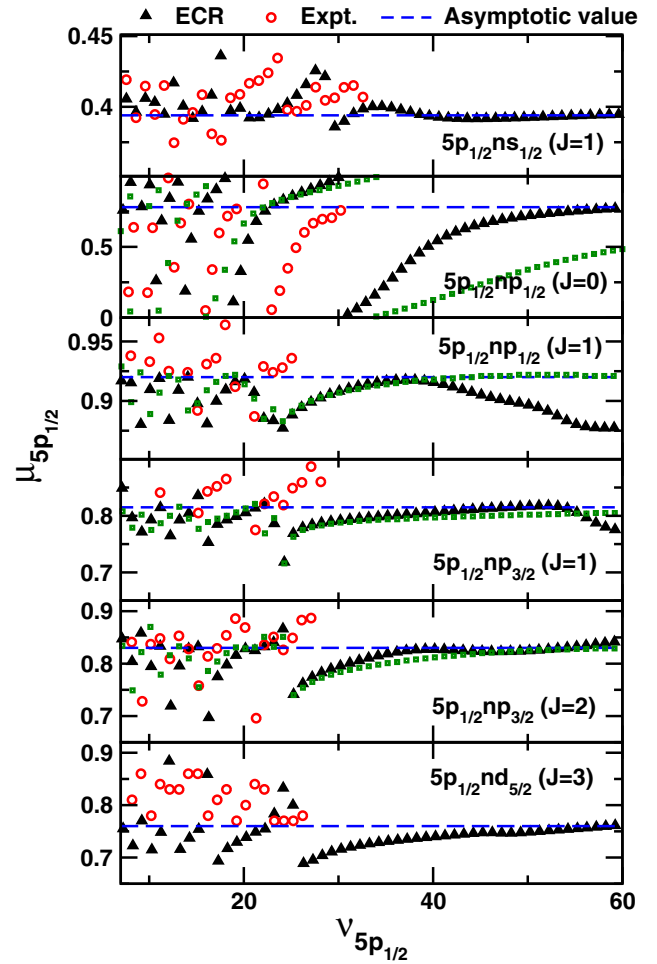


FIG. 6. Quantum defects of $\mu_{5p_{1/2}} = \lceil v_{5p_{1/2}} \rceil - v_{5p_{1/2}}$ for $5p_{1/2}ns_{1/2}$, $5p_{1/2}np_j$, and $5p_{1/2}nd_j$ autoionizing states calculated by the ECR method (triangles) and measured values (open circles) ($5p_{1/2}ns_{1/2}$ from [31], $5p_{1/2}np_j$ from [33] and $5p_{1/2}nd_j$ from [32]). The dashed lines are the fitted asymptotic values.

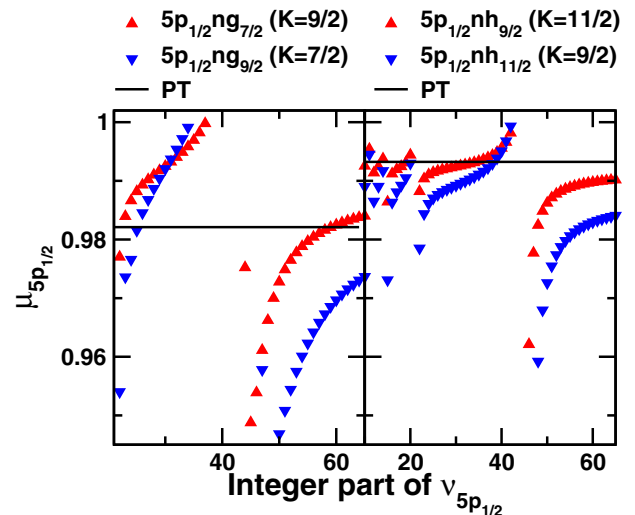


FIG. 7. Quantum defect of $5p_{1/2}ng_j (J = \ell)$ and $5p_{1/2}nh_j (J = \ell)$ series of autoionizing states calculated by the ECR method (triangles) and by perturbation theory (PT, solid line). Note the expanded scale of the $\mu_{5p_{1/2}}$ axis.

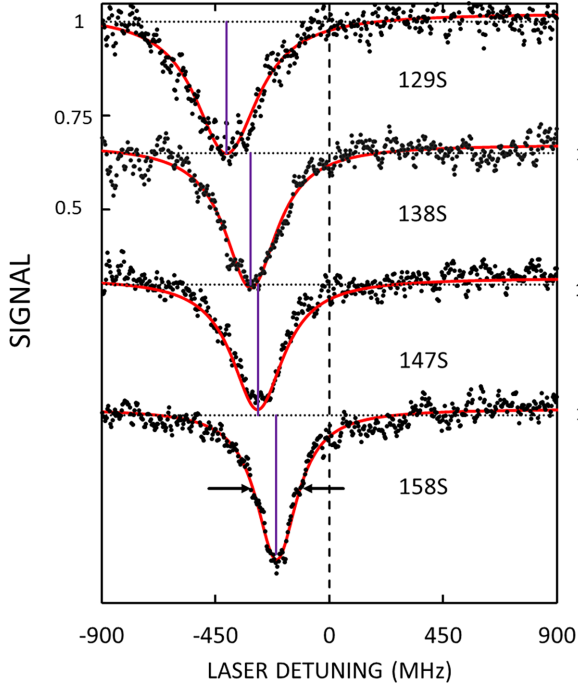


FIG. 8. n dependence of the autoionization loss profiles for singly excited $5sns\ ^1S_0$ Rydberg atoms. Each data set is normalized to the total initial number of Rydberg atoms created and for each value of n the 422-nm laser power was adjusted to achieve similar fractional peak losses. A Lorentzian fit (red solid line) to each profile with line centers (dotted lines) and widths Γ (arrows) indicated is included.

the shifts in the core ion $5s_{1/2}\ ^2S_{1/2} - 5p_{1/2}\ ^2P_{1/2}$ transition frequencies (from that of a bare Sr^+ ion) are plotted in Fig. 9 as a function of the effective quantum number ν_{5s} of the initial Rydberg state for several values of ℓ . The line-center shifts Δ_L can be well approximated as

$$\Delta_L = -\frac{1}{2\nu_{5p_{1/2}}^2} + \frac{1}{2\nu_{5s}^2} \approx \frac{\nu_{5p_{1/2}} - \nu_{5s}}{\nu_{5s}^3}. \quad (22)$$

Correspondingly, the effective quantum numbers of the autoionizing states are determined by $\nu_{5p_{1/2}} \approx \nu_{5s} + \nu_{5s}^3 \Delta_L$ and the fractional part of the quantum defect is $\mu_{5p_{1/2}} \approx [\nu_{5s}] - \nu_{5s} - \nu_{5p_{1/2}}$. In the high- n limit the quantum defect reaches the asymptotic value and $\nu_{5p_{1/2}} - \nu_{5s}$ becomes nearly constant. The widths w can be well fit by an expression of similar form

$$w = \Gamma_0 / \nu_{5p_{1/2}}^3 + \Delta\omega_0, \quad (23)$$

where $\Delta\omega_0$ (≈ 21.7 MHz) is the radiative decay rate of the $5p_{1/2}$ state of an Sr^+ ion. The fitted values of quantum defect $\mu_{5p_{1/2}}$ and Γ_0 are listed in Table II. Representative autoionization loss spectra recorded for singly excited states $5sn\ell$ with different values of ℓ are shown in Fig. 10(a). Since several autoionizing states are optically accessible from a given singly excited state with $\ell > 0$, the measured spectra become a sum of several Lorentzian profiles. Since the integral over the Lorentzian is proportional to the oscillator strength, autoionizing states with larger dipole transition strengths and smaller decay rates are expected to be more prominent, i.e., the depth of each Rydberg atom loss feature is expected to be

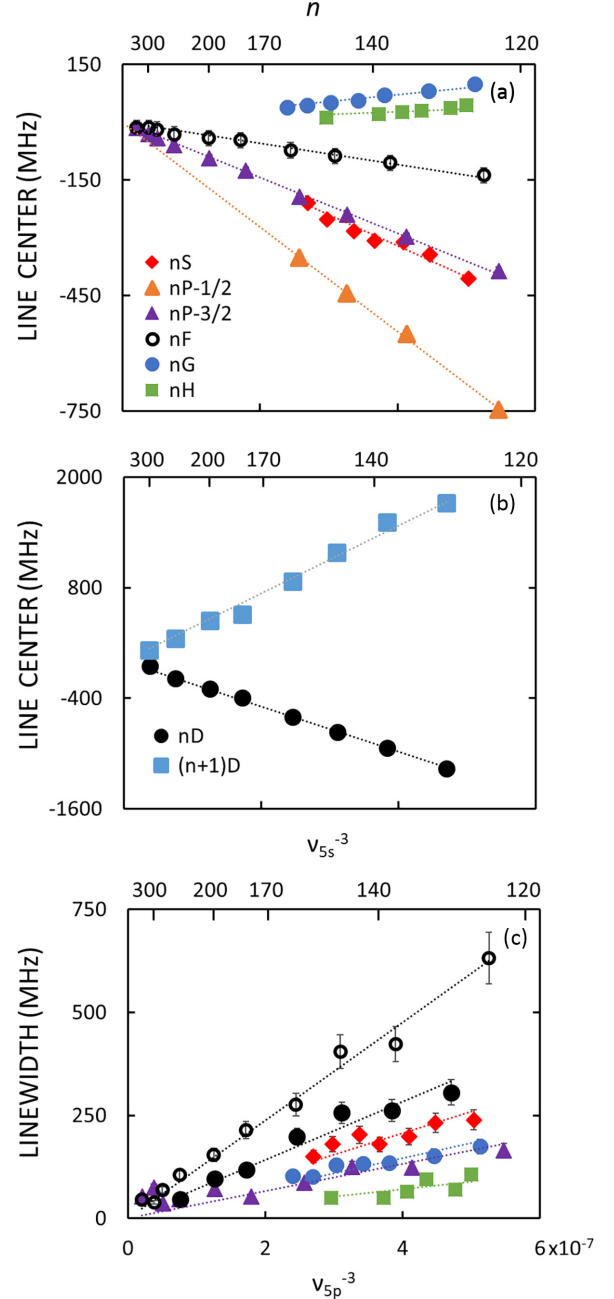


FIG. 9. Line center shifts for (a) $\ell \neq 2$ and for (b) $\ell = 2$ and (c) values of $w - \Delta\omega_0$ extracted from the measured autoionization loss spectra for $\ell \leq 5$. For $\ell = 1$, the line-center shifts associated with the two atom loss features corresponding to $j = 1/2$ and $3/2$ are extracted (see the text for details), but the width is extracted only from the larger ($j = 3/2$) feature. Since the line-center shifts for $\ell = 2$ are much larger than for other ℓ , they are shown separately in (b) which includes the features seen at both negative and positive detuning. The width is extracted only from the larger feature at negative detuning. The dashed lines are the fits to the measured data [Eqs. (22) and (23)]. In (a) and (b) the size of the data points indicates the size of the measurement uncertainties.

proportional to the squared dipole transition matrix element and inversely proportional to Γ .

The dipole transition matrix elements can be evaluated by expanding each autoionizing state $|(5p_{1/2}n\ell_j)JM_J\rangle$ in terms

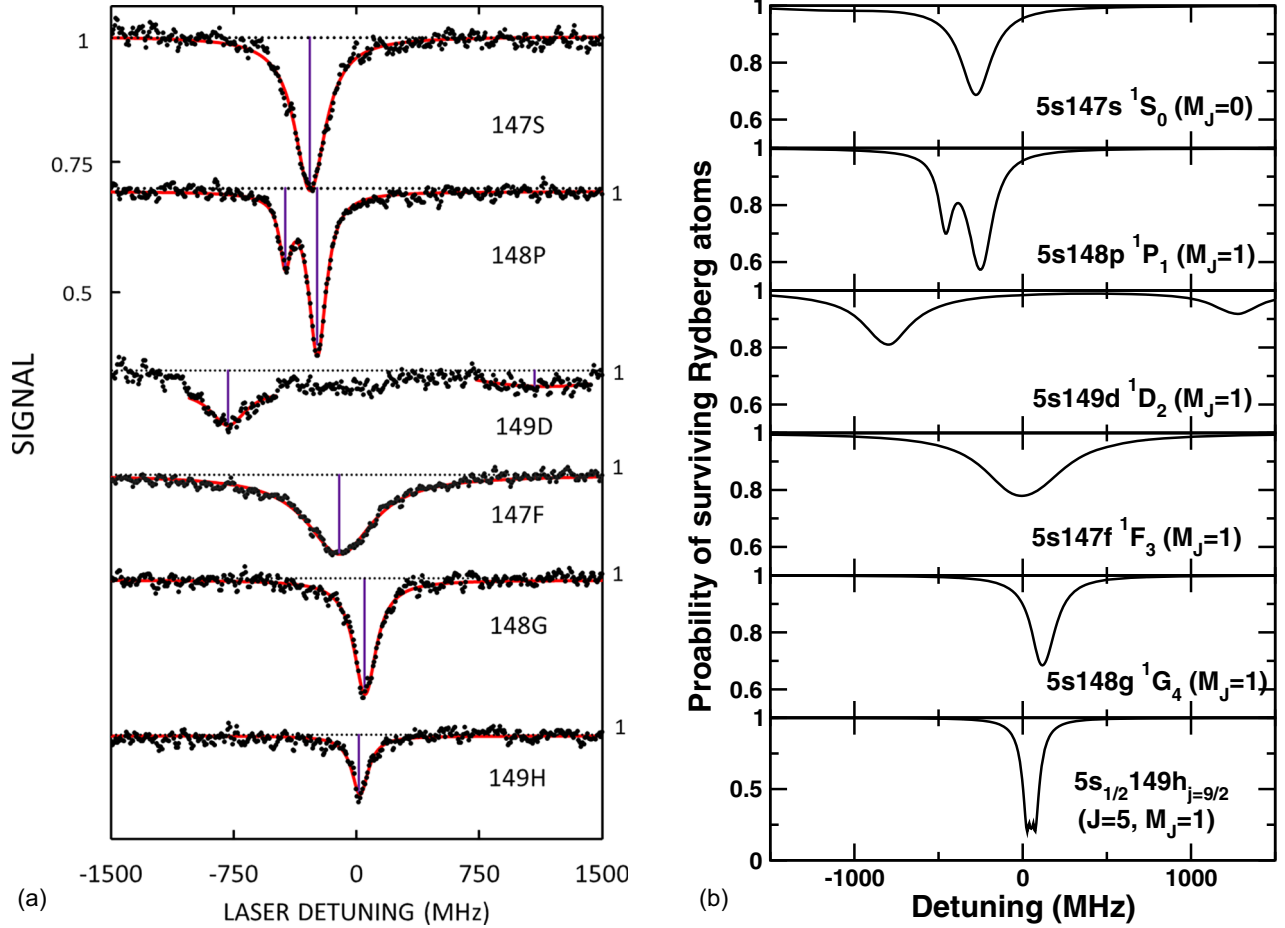


FIG. 10. (a) Autoionization loss profiles recorded for the states indicated. The spectra were obtained using identical 422-nm laser powers and pulse durations and each data set is normalized to the initial number of Rydberg atoms created. A Lorentzian fit (red solid line) to each profile is included. (b) Simulated survival probability of Rydberg atoms representing autoionization loss profiles for the states indicated.

of the unperturbed basis [Eq. (7)]. The dipole transition matrix elements between unperturbed basis states are given by

$$\begin{aligned} \langle 0 | \langle (5p_{1/2} n' \ell_j) J' M_J | z_v | \langle (5s_{1/2} n \ell_j) J M_J \rangle_0 \rangle \simeq & -\frac{1}{3} \langle 5p | r | 5s \rangle \langle 5p | n' \ell | n \ell \rangle_{5s} \times \left[\delta_{j, \ell-1/2} \left(\frac{\sqrt{(J-M_J)(J+M_J)}}{J} \delta_{J', J-1} + \frac{M_J}{J} \delta_{J', J} \right) \right. \\ & \left. + \delta_{j, \ell+1/2} \left(-\frac{M_J}{J+1} \delta_{J', J} + \frac{\sqrt{(J'-M_J)(J'+M_J)}}{J'} \delta_{J', J+1} \right) \right]. \end{aligned} \quad (24)$$

In Eq. (24) the magnetic quantum number M_J is defined relative to the laser polarization taken to be the quantization axis. The overlap $\langle 5p | n' \ell | n \ell \rangle_{5s}$ in Eq. (24) does not vanish [49] since the Rydberg states n and n' are associated with different effective ionic cores [Eq. (10)]. Typically, the initial singly excited states with the $5s$ inner valence electron are well represented by the LS coupling scheme since the spin-orbit coupling is negligibly small. In this case, the matrix elements in the jj coupling representation [Eq. (24)] need to be transformed to the LS basis where the transition is given by a Wigner $9j$ symbol [50]. However, for $\ell > 4$ the singly excited states are well represented by the jj -coupling scheme [50,51] and no transformation is required. The selection rules for the inner valence electron excitation are $|\Delta \ell_v| = 1$ and

$|\Delta J| \leq 1$. In the limit of large J , the two valence electrons become uncorrelated and the latter selection rule is reduced to $|\Delta J| = 1$ and the $J' = J$ states will not be populated.

Using the calculated dipole matrix elements and complex eigenenergies (the imaginary part representing $\Gamma/2$), the photoexcitation of the inner valence electron by a $1 \mu\text{s}$ laser pulse from the initial singly excited Rydberg atom is simulated using the rotating wave approximation. The probability of remaining in the initial Rydberg state after the excitation pulse followed by autoionization is shown in Fig. 10(b). Since the initial 1P_1 and 1F_3 singly excited states are prepared in the absence of the microwave field, the magnetic quantum numbers (quantized along the z axis) $|M_J| = 1$ for 1P_1 and $|M_J| = 1$ or 3 for 1F_3 are well defined. Due to the experimental uncertainty

in the microwave polarization, the magnetic quantum numbers M_J of the initial singly excited Rydberg states for $\ell \neq 1, 3$ are unknown. In the simulation, we set the magnetic quantum number of the initial Rydberg states to $M_J = 0$ for the 1S_0 state and to $M_J = 1$ for all other $\ell > 0$ states. The autoionizing loss spectra are insensitive to M_J of the initial state except for large M_J when some autoionizing states with $J < |M_J|$ cannot be reached.

Starting from the $5s147s\ ^1S_0$ state, the $5p_{1/2}v_{5p_{1/2}}s_{1/2}$ ($J = 1$) autoionizing state with effective quantum number $v_{5p_{1/2}} \simeq 143.6$ is predominantly excited. As discussed earlier, due to configuration mixing, the $5p_{1/2}v_{5p_{1/2}}d_{3/2}$ ($J = 1$) state has a small admixture of the $|(5p_{1/2}v_{5p_{1/2}}s_{1/2})J = 1\rangle_0$ state and can be excited from the singly excited 1S_0 Rydberg state as well. However, this admixture is small and the width Γ large (Table II). Consequently, the $\ell = 2$ state contributes only as a shallow and broad dip which is barely visible in the plot. As a result, the measured Γ_0 and $\mu_{5p_{1/2}}$ closely resemble the calculated values for the $5p_{1/2}v_{5p_{1/2}}s_{1/2}$ ($J = 1$) autoionizing state. Indeed the measured autoionization rate agrees with the ECR calculation within the error of 0.01 (corresponding to ~ 20 MHz at $v_{5p_{1/2}} = 150$) and is consistent with the measurement for low n (Fig. 3). Similarly, the quantum defect agrees reasonably well (Table II).

Starting from the $5s148p\ ^1P_1$ ($M_J = 1$) state, two atom loss peaks are observed. While the $5p_{1/2}v_{5p_{1/2}}p_{1/2}$, $J = 0$ state is optically inaccessible for $M_J = 1$, the calculated quantum defects $\mu_{5p_{1/2}}$ are larger for the $5p_{1/2}v_{5p_{1/2}}p_{1/2}$, $J = 1$ state than for the other two $5p_{1/2}v_{5p_{1/2}}p_{3/2}$, $J = 1, 2$ states. Consequently, the autoionizing state $5p_{1/2}v_{5p_{1/2}}p_{1/2}$, $J = 1$ gives rise to a shallow loss feature around -450 MHz and the $5p_{1/2}v_{5p_{1/2}}p_{3/2}$, $J = 1, 2$ states to a more pronounced loss feature near -300 MHz. Since the difference in quantum defect (~ 0.1) between $j = 1/2$ and $3/2$ is comparable to the width Γ_0 , they partially overlap. Each feature is fitted separately (Table II) and the agreement between the measured data for low n and the ECR calculation is comparable to that for the $\ell = 0$ state. For $\ell = 2$, Rydberg atom loss features are evident at both positive and negative detunings (see Fig. 11 and [13,32]). By determining the occupation probabilities predicted by the ECR calculation projected onto the unperturbed basis, they can be identified as the $5p_{1/2}nd_j$ and $5p_{1/2}(n+1)d_j$ autoionizing states. These multiple peaks are due to the nonnegligible overlap ${}_S\langle n'\ell|n\ell\rangle_{SS}$ even when the principal quantum numbers differ, $n' \neq n$ [Eq. (24)]. Indeed, the atom loss spectra measured for several values of n show that the separation of the two peaks agrees well with the energy difference between adjacent n levels, i.e., ~ 3 GHz at $n = 131$, ~ 2 GHz at $n = 150$, and ~ 1 GHz at $n = 182$. (Note that the laser powers were again chosen to obtain similar fractional peak losses of $\sim 30\%$. However, the powers required to induce these losses were significantly larger than those required to produce similar losses for the other ℓ states.) Moreover, atom losses are seen at large detunings which are comparable to $1/v^3$ indicating that the autoionizing state excited has an effective quantum number very different from that of the initial singly excited state. This significant change in the effective quantum number is caused by the relatively large energy splitting between the singlet and triplet states of the singly excited

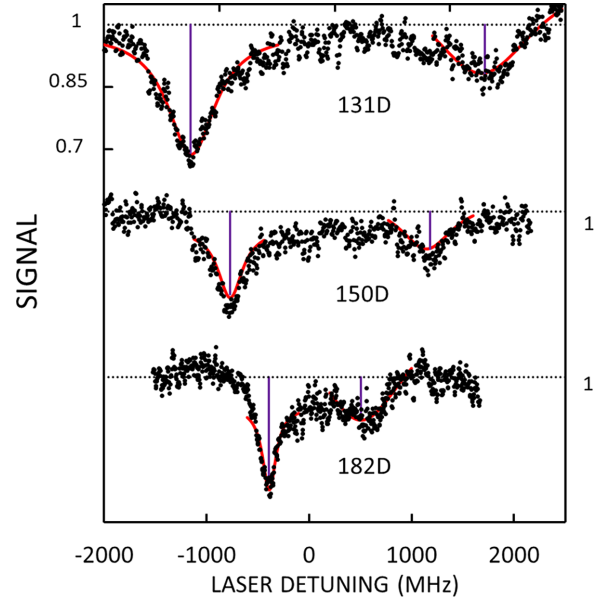


FIG. 11. n dependence of the autoionization loss profiles for singly excited $5snd\ ^1D_2$ Rydberg atoms. For each value of n the 422-nm laser power was adjusted to achieve similar peak losses. A fit to each loss feature using a Lorentzian is included (red solid line).

$5snd$ Rydberg states ($\mu = 2.38$ for $S = 0$ and $\mu = 2.66$ for $S = 1$) [52,53]. This is different from the other ℓ levels for which the fine-structure splittings are smaller. The width and line center can be extracted from the measured spectra for each peak separately. The fitted values of Γ_0 and $\mu_{5p_{1/2}}$ are nearly the same for the both peaks (Table II). Each atom loss peak of the $5p_{1/2}nd_j$ autoionizing state includes contributions from states with different values of j and J with the oscillator strengths being largest for $J = 1$ and 3 states [Eq. (24)]. Since the calculated autoionization rate is much smaller for $J = 3$ than for $J = 1$, the atom loss contains a narrow and deep dip from the excitation of the $J = 3$ autoionizing state and a broad and shallow dip from excitation of the $J = 1$ state. Therefore, the autoionization rate and the quantum defect of the $J = 3$ autoionizing state are most easily extracted from the measured spectra. This tendency is even enhanced when the initial singly excited state has significant $|M_J| = 2$ components for which the dipole transition to $J = 1$ states is forbidden. Indeed, the fitted values of Γ_0 and $\mu_{5p_{1/2}}$ are close to those of the $J = 3$ autoionizing states while small deviations are caused by the contributions from the $J = 1, 2$ autoionizing states.

With further increases in ℓ , the dipole transition to the autoionizing states with $J = \ell$ are suppressed and the $J = \ell \pm 1$ states become dominant. For $\ell = 3$, the large autoionization rate of the individual J levels results in relatively broad atom loss feature. Additionally, the width $\Gamma_0 \sim 0.2$ is much larger than the energy difference between the autoionizing states of $J = 2$ and $J = 4$ ($\Delta\mu \simeq 0.07$). These two states cannot be resolved in the measured spectra and the effective width of the atom loss peak, which includes the contributions from both autoionizing states, will be only slightly broadened by the splitting $\Delta\mu$. Indeed, the measured value of Γ_0 agrees quite well with the calculations. For $\ell \geq 4$, the excited Ry-

berg electron is simply a spectator during the excitation of the inner valence electron and modifications in the outer electron wave function are expected to be small. Therefore, in this so-called isolated core excitation regime, the oscillator strength becomes approximately that for excitation of a bare Sr^+ ion [Eq. (24)] and largely independent of $\nu_{5p_{1/2}}$ and ℓ . Since the autoionization rates decrease with ℓ , narrower and more pronounced loss features are expected. This is seen for the Rydberg atom loss spectrum of the $5s148g$ state. Calculations indicate that this trend continues for $\ell = 5$. However, the measured loss for the $5s149h$ state appears to be significantly smaller than that for the $5s148g$ state implying that the excitation probability for the inner valence electron is suppressed for the $5s149h$ state compared to that of the $5s148g$ state. Discrepancies between the measured data and the nonperturbative calculation are also found in the quantum defects for the autoionizing states with $\ell = 4$ and 5. The calculated quantum defects (defined as modulo 1) reflects the negative polarizability of Sr^+ ion [46,47] and the energy levels are blue-shifted from the hydrogenic level while the measured quantum defects indicate the red-shifted energy levels (Table II). Differences are seen but are very small, and when translated to effective quantum numbers, amount to $\lesssim 0.02$ requiring a higher accuracy in both experiment and theory (e.g., more accurate model potentials) to resolve this discrepancy.

Overall, the measured autoionization rates exhibit a power-law scaling of $\nu_{5p_{1/2}}^{-3}$. This scaling with $\nu_{5p_{1/2}}$ is intuitive in that the autoionization rate decreases as the electron-electron interaction becomes weak for large n . Whereas at low n the calculated rates fluctuate due to the presence of intruder states, the calculated autoionization rates do agree well with the measurements (Table II) if Γ_0 is fit to the lower limit of these fluctuations. Currently, convergence in the calculation of the autoionization rates can be achieved for $\nu_{5p_{1/2}} \lesssim 60$.

In contrast, the autoionization rates do not display a simple monotonic behavior as ℓ is increased, as shown in Fig. 12(a), for the lower values of ℓ . Figure 12 also includes the prediction from [20]

$$\Gamma = \frac{\pi\alpha_d}{2(\ell + 3/2)(\ell + 1)(\ell + 1/2)\ell(\ell - 1/2)}, \quad (25)$$

which is valid for high- ℓ states. Naively, it might be expected that with increasing ℓ the centrifugal barrier would increasingly limit core penetration by the Rydberg electron, whereupon, the electron-electron interactions and autoionization rates would decrease steadily. The autoionization rate [Eq. (12)], however, is influenced by the radial integral ${}_{5s(4d)}\langle \epsilon, \ell' | r^{-2} | n, \ell \rangle_{5p}$ involved in the direct amplitude A_d [Eq. (14)]. At large r the scattering state $|\epsilon, \ell'\rangle$ is a rapidly oscillating function while the bound state $|n, \ell\rangle$ is slowly oscillating. Therefore, the radial integral is determined by the behavior at small r . Whereas the radial integral decreases with increasing ℓ due to the centrifugal barrier, the phase shift $\mu^{(0)}$ induced by the effective ion core [Eq. (10)] also affects the integral. Indeed, phase matching between the bound and scattering wave functions at small distances ($r \simeq 10$ a.u.) for $\ell = 2$ and 3 states enhances the radial integral as well as the autoionization rate. On the other hand, the differences in phase shifts suppresses the autoionization rate for $\ell = 0$ and 1. This

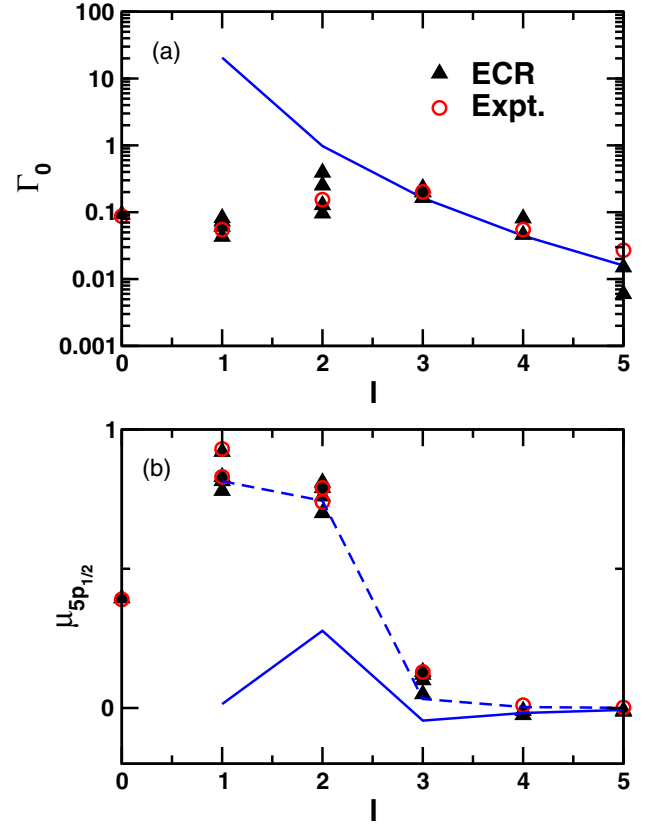


FIG. 12. ℓ dependence of (a) Γ_0 and (b) $\mu_{5p_{1/2}}$: the measured data (open circles), the ECR calculations (filled triangles), and the prediction [Eq. (25)] from [20] (solid line). The dashed line in (b) indicates the quantum defect $\mu^{(0)}$ without the second-order correction [Eq. (17)].

phase (mis)match is at the core of the nonmonotonic behavior of Γ_0 as a function of ℓ . Similarly, the measured quantum defect can also be compared with the prediction [Eqs. (16) and (17)] for high- ℓ states. [We note that Fig. 12(b) shows only the fractional part of the quantum defect. The quantum defect including the integer part may decrease monotonically with ℓ .] For low- ℓ states, the quantum defect is well approximated by the phase shift $\mu^{(0)}$ induced by the effective ion core and higher-order corrections appear to be much smaller than those predicted by Eq. (16) for $\mu^{(2)}$. For $\ell \geq 4$, however, the zeroth-order correction $\mu^{(0)}$ becomes negligible and, as expected, the quantum defects are well approximated by the second-order corrections [Eq. (16)].

V. CONCLUSION

We experimentally and theoretically investigated the n and ℓ dependence of the autoionization rates of doubly excited ${}^{88}\text{Sr}$ high Rydberg states. Autoionization rates Γ and quantum defects $\mu_{5p_{1/2}}$ for such states are calculated within a quasi-two-electron description employing the exterior complex rotation method and the results compared to the experimental data and the predictions of perturbation theory. As expected, the autoionization rates decrease with increasing effective quantum number $\nu_{5p_{1/2}}$ ($\sim n$) as $\sim \Gamma_0/\nu_{5p_{1/2}}^3$. This scaling emerges,

however, only for large n where the distortion introduced by intruder states has subsided. For lower n the presence of intruder states requires great care when extracting the asymptotic value of Γ_0 for a given series. The values of Γ_0 found using ECR calculations and experiment agree well but differ from those provided by perturbation theory because of configuration mixing and exchange effects not included in the perturbative approach. The ℓ dependence of the autoionizing rates was found to be nonmonotonic. For high values of ℓ , the autoionization rate decreases as ℓ^{-5} due to the centrifugal barrier which prevents the outer electron from penetrating the core and the inner valence electron cloud. In this regime autoionization is found to be well described by the perturbative approximation. For low- ℓ core-penetrating states, the scattering phase shift $\mu^{(0)}$ associated with the effective core potential, which includes the screening effects of the inner

valence electron, plays an important role in determining both autoionization rates and quantum defects. In particular, the local maximum in the rate near $\ell \simeq 2-3$ was found to be the consequence of phase matching between the bound and the scattering wave functions, which is not accounted for in a perturbative approach. Similar trends can be observed for quantum defects. Whereas, for high ℓ , perturbation theory and the nonperturbative ECR calculation tend to agree, significant discrepancies are seen for low to intermediate ℓ .

ACKNOWLEDGMENTS

Research supported by the NSF (Grant No. 1904294), and the FWF (Austria) (Grants No. FWF-P35539-N and No. FWF-W1243 Doctoral College). The Vienna scientific cluster was used for the calculations.

-
- [1] C. S. Adams, J. D. Pritchard, and J. P. Shaffer, *J. Phys. B* **53**, 012002 (2019).
- [2] M. Saffman, T. G. Walker, and K. Mølmer, *Rev. Mod. Phys.* **82**, 2313 (2010).
- [3] T. F. Gallagher, *J. Opt. Soc. Am. B* **4**, 794 (1987).
- [4] W. E. Cooke, T. F. Gallagher, S. A. Edelstein, and R. M. Hill, *Phys. Rev. Lett.* **40**, 178 (1978).
- [5] A. P. Burgers, S. Ma, S. Saskin, J. Wilson, M. A. Alarcón, C. H. Greene, and J. D. Thompson, *PRX Quantum* **3**, 020326 (2022).
- [6] A. Muni, A. Lachaud, A. Couto, M. Poirier, R. C. Teixeira, J.-M. Raimond, M. Brune, and S. Gleyzes, *Nat. Phys.* **18**, 502 (2022).
- [7] R. Mukherjee, J. Millen, R. Nath, M. P. A. Jones, and T. Pohl, *J. Phys. B* **44**, 184010 (2011).
- [8] J. T. Wilson, S. Saskin, Y. Meng, S. Ma, R. Dilip, A. P. Burgers, and J. D. Thompson, *Phys. Rev. Lett.* **128**, 033201 (2022).
- [9] K.-L. Pham, T. F. Gallagher, P. Pillet, S. Lepoutre, and P. Cheinet, *PRX Quantum* **3**, 020327 (2022).
- [10] P. McQuillen, X. Zhang, T. Strickler, F. B. Dunning, and T. C. Killian, *Phys. Rev. A* **87**, 013407 (2013).
- [11] D. Wehrli, M. Génévriez, and F. Merkt, *Phys. Rev. A* **100**, 012515 (2019).
- [12] U. Fano and J. W. Cooper, *Phys. Rev.* **137**, A1364 (1965).
- [13] J. Millen, G. Lochead, and M. P. A. Jones, *Phys. Rev. Lett.* **105**, 213004 (2010).
- [14] I. S. Madjarov, J. P. Covey, A. L. Shaw, J. Choi, A. Kale, A. Cooper, H. Pichler, V. Schkolnik, J. R. Williams, and M. Endres, *Nat. Phys.* **16**, 857 (2020).
- [15] R. Brienza, G. Fields, and F. B. Dunning, *Rev. Sci. Instrum.* **92**, 075105 (2021).
- [16] G. Fields, X. Zhang, F. B. Dunning, S. Yoshida, and J. Burgdörfer, *Phys. Rev. A* **97**, 013429 (2018).
- [17] J. Dubau and S. Volonte, *Rep. Prog. Phys.* **43**, 199 (1980).
- [18] D. S. Belic, G. H. Dunn, T. J. Morgan, D. W. Mueller, and C. Timmer, *Phys. Rev. Lett.* **50**, 339 (1983).
- [19] Z. Harman, C. Shah, A. J. González Martínez, U. D. Jentschura, H. Tawara, C. H. Keitel, J. Ullrich, and J. R. Crespo López-Urrutia, *Phys. Rev. A* **99**, 012506 (2019).
- [20] W. E. Cooke and T. F. Gallagher, *Phys. Rev. A* **19**, 2151 (1979).
- [21] U. Eichmann, V. Lange, and W. Sandner, *Phys. Rev. Lett.* **68**, 21 (1992).
- [22] M. Génévriez, C. Rosen, and U. Eichmann, *Phys. Rev. A* **104**, 012812 (2021).
- [23] M. Poirier, *Phys. Rev. A* **38**, 3484 (1988).
- [24] N. H. Tran, P. Pillet, R. Kachru, and T. F. Gallagher, *Phys. Rev. A* **29**, 2640 (1984).
- [25] J. Boulmer, P. Camus, and P. Pillet, *J. Opt. Soc. Am. B* **4**, 805 (1987).
- [26] J. Boulmer, P. Camus, J.-M. Lecomte, and P. Pillet, *J. Opt. Soc. Am. B* **5**, 2199 (1988).
- [27] R. D. Verma and A. Chanda, *J. Opt. Soc. Am. B* **5**, 86 (1988).
- [28] P. Camus, T. F. Gallagher, J.-M. Lecomte, P. Pillet, L. Pruvost, and J. Boulmer, *Phys. Rev. Lett.* **62**, 2365 (1989).
- [29] G. Waligorski, L. Zhou, and W. E. Cooke, *Phys. Rev. A* **55**, 1544 (1997).
- [30] H. Lehec, X. Hua, P. Pillet, and P. Cheinet, *Phys. Rev. A* **103**, 022806 (2021).
- [31] E. Y. Xu, Y. Zhu, O. C. Mullins, and T. F. Gallagher, *Phys. Rev. A* **33**, 2401 (1986).
- [32] E. Y. Xu, Y. Zhu, O. C. Mullins, and T. F. Gallagher, *Phys. Rev. A* **35**, 1138 (1987).
- [33] S. Cohen, M. Aymar, A. Bolovinos, M. Kompitsas, E. Luc-Koenig, H. Mereu, and P. Tsekeris, *Eur. Phys. J. D* **13**, 165 (2001).
- [34] R. C. Teixeira, A. Larrouy, A. Muni, L. Lachaud, J.-M. Raimond, S. Gleyzes, and M. Brune, *Phys. Rev. Lett.* **125**, 263001 (2020).
- [35] J. H. Van Vleck and N. G. Whitelaw, *Phys. Rev.* **44**, 551 (1933).
- [36] U. Fano, *Phys. Rev.* **124**, 1866 (1961).
- [37] W. E. Cooke and C. L. Cromer, *Phys. Rev. A* **32**, 2725 (1985).
- [38] B. Simon, *Phys. Lett. A* **71**, 211 (1979).
- [39] A. Sinclair, M. Wilson, and P. Gill, *Opt. Commun.* **190**, 193 (2001).
- [40] R. F. Stebbings and F. B. Dunning, *Rydberg States of Atoms and Molecules* (Cambridge University Press, Cambridge, England, 1983).

- [41] T. F. Gallagher, *Rydberg Atoms* (Cambridge University Press, New York, 1994).
- [42] S. Ye, X. Zhang, F. B. Dunning, S. Yoshida, M. Hiller, and J. Burgdörfer, *Phys. Rev. A* **90**, 013401 (2014).
- [43] G. Wentzel, *Z. Phys.* **43**, 524 (1927).
- [44] E. Fermi, *Nuclear Physics: A Course Given by Enrico Fermi at the University of Chicago* (University of Chicago Press, Chicago, 1950).
- [45] R. R. Freeman and D. Kleppner, *Phys. Rev. A* **14**, 1614 (1976).
- [46] M. Aymar, R. Guérout, and O. Dulieu, *J. Chem. Phys.* **135**, 064305 (2011).
- [47] J. Mitroy, J. Y. Zhang, and M. W. J. Bromley, *Phys. Rev. A* **77**, 032512 (2008).
- [48] R. D. Cowan, *The Theory of Atomic Structure and Spectra* (University of California Press, Berkeley, CA, 1981).
- [49] S. A. Bhatti, C. L. Cromer, and W. E. Cooke, *Phys. Rev. A* **24**, 161 (1981).
- [50] G. Fields, R. Brienza, F. B. Dunning, S. Yoshida, and J. Burgdörfer, *Phys. Rev. A* **104**, 032817 (2021).
- [51] J. Nunkaew, E. S. Shuman, and T. F. Gallagher, *Phys. Rev. A* **79**, 054501 (2009).
- [52] P. Esherick, *Phys. Rev. A* **15**, 1920 (1977).
- [53] R. Ding, J. D. Whalen, S. K. Kanungo, T. C. Killian, F. B. Dunning, S. Yoshida, and J. Burgdörfer, *Phys. Rev. A* **98**, 042505 (2018).